Orthotropic 3D elastic plastic non-local CDM model for wood validation with multiple test cases

Seeber, Franziska; Khaloian-Sarnaghi, Ani; Benvenuti, Elena; van de Kuilen, Jan Willem

DOI
10.1007/s00226-025-01685-z

Publication date
2025

Document Version
Final published version

Published in
Wood Science and Technology

Citation (APA)
Seeber, F., Khaloian-Sarnaghi, A., Benvenuti, E., & van de Kuilen, J. W. (2025). Orthotropic 3D elastic plastic non-local CDM model for wood: validation with multiple test cases. *Wood Science and Technology*, *59*(6), Article 104. https://doi.org/10.1007/s00226-025-01685-z

Wood Science and Technology (2025) 59:104
https://doi.org/10.1007/s00226-025-01685-z

ORIGINAL

Orthotropic 3D elastic plastic non-local CDM model for wood: validation with multiple test cases

Franziska Seeber[1] · **Ani Khaloian-Sarnaghi**[1] · **Elena Benvenuti**[2] ·
Jan-Willem van de Kuilen[1,3]

Received: 20 August 2024 / Accepted: 16 July 2025

Abstract

This contribution aims to increase the understanding of the complex mechanical behavior of wood through a framework for simulating mixed-mode failure. Based on physical properties assessment, appropriate constitutive laws, and experimental validation, a generally applicable numerical strength prediction tool for wood from different species and with various natural imperfections is introduced. The 3D orthotropic elastic plastic non-local CDM model considers the local fiber orientation and is implemented as material subroutines in the commercial software Abaqus. Herein, orthotropic Hill-plasticity with exponential hardening represents the plastic behavior in compression. Separated stress-based gradient-enhanced transient non-local damage represents the brittle material behavior in tension and shear. The methodology is validated with experimental data on tensile veneer tests, shear- and compression tests. Moreover, the methodology is applied to four-point bending tests of boards with heterogeneities. The numerical results demonstrate that the proposed model is able to reproduce different crack patterns observed in the four-point bending tests. Detailed investigations of the impact on the strength of the boards can be performed with this method to optimize species-independent strength prediction and engineered wood products. Further combination with other material laws e.g. moisture is possible.

Introduction

Prediction of fracture behavior and the strength of wood and wood-based materials is crucial before wood is used in engineering applications. Such predictions may help to optimize engineered wood products. Recently, numerical methods have been introduced aiming to contribute to the testing of wood and providing important insights into crack growth prediction of the complex and naturally grown material.

Extended author information available on the last page of the article

As an alternative to discrete approaches such as cohesive zone models (Ortiz and Pandolfi 1999) or XFEM approaches (Moës and Belytschko 2002), continuum damage mechanics (CDM) approaches (Lemaître and Desmorat 2005) model discontinuities in a continuum. Still, local CDM suffers mesh dependency problems and is thus enhanced to non-local CDM modifying the Helmholtz free energy and allowing for an exchange of energy in a certain interaction region (Peerlings et al. 1996) for fracture modeling. Similarly, the currently popular phase-field method (Ambati et al. 2014; Francfort and Marigo 1998) introduces an additional crack phase-field which is based on an energy minimization problem.

Specifically for wood several numerical methods to approach fracture were developed in literature. While discrete approaches such as cohesive zone models (Danielsson and Gustafsson 2016; Resch and Kaliske 2010), and XFEM (Lukacevic et al. 2015; Benvenuti and Orlando 2021) are dependent on an a priori known crack path, and only convenient for limited cases, local CDM approaches (Sandhaas 2012) suffer from pathological mesh dependence. Non-local damage (Shala and Waisman 2024) overcomes this by introducing a localizing gradient damage formulation for the non-local damage regularization. Alternatively, the phase-field approach has been recently enhanced for predicting the fracture behavior of wood through anisotropic mode-dependent phase-field evolution (Supriatna et al. 2022; Pech et al. 2022).

Strength prediction of wooden boards is mostly based on visual grading criteria, while a huge amount of information about local fiber patterns and other physical properties is available from machine grading. On the numerical side, simulation methods that combine mechanical material laws (Wang et al. 2018; Benvenuti et al. 2020) are mainly developed for transversely isotropic clear wood or only model wooden boards with imperfections in the elastic material range (Lukacevic et al. 2019; Khaloian Sarnaghi and van de Kuilen 2019). Generally, for numerically predicting the material behavior of wood, it is important to include the orthotropic material character as well as the local fiber pattern of the naturally grown fiber composite. Different failure modes evolve depending on fiber orientation and loading state and can be represented by different constitutive laws, such as e.g. damage, plasticity, viscoelasticity, or mechano-sorption. A validated simulation tool is thus beneficial to allow e.g. strength prediction by combining local material properties with elastic and post-elastic constitutive laws for wooden boards independent of the wood species. A systematically performed validation of the simulation tool on experimentally tested samples is necessary for developing such generally applicable virtual strength prediction tool.

In this contribution, non-local CDM is developed in a commercial FE solver, because of its computational efficiency (Zhang et al. 2022). Moreover, it entails operational benefits for solving various examples with optional additional material laws such as plasticity. Non-local damage was initially developed for isotropic materials based on an equivalent strain (Peerlings et al. 1996), and is lately enhanced for orthotropic materials introducing stress-based damage initiation criteria (Seeber et al. 2025) or even for wood (Shala and Waisman 2024). It reflects the evolution of micro-cracks to an accumulated macro-crack using a transient interaction function (Poh and Sun 2017) and thus restricts the fracture process zone to a thin crack. Finally, non-local CDM has recently been combined with neuronal networks for an accelerated numerical solution (Pantidis and Mobasher 2023).

In Seeber et al. (2025), the 3D orthotropic elastic plastic non-local CDM model uses a transient localizing implicit gradient formulation for damage. It initiates several stress-based damage variables with the decisive failure mode regularized non-locally. This allows the representation of the orthotropic material behavior with a clear failure mode distinction. The simulation is performed using a commercial solver Abaqus which allows an enhancement of the method for an efficient simulation of 3D examples, straight-forward inclusion of local fiber orientations, and the combination of non-local damage with orthotropic plasticity in this study.

Validation of the developed method is initially performed on clear wood samples in 2D. Step by step more complexity is added to the model and the models are validated in 3D. Finally, the fracture behavior of wooden boards with specific types of imperfections, including fiber deviations and different knot types and shapes, is investigated both experimentally and numerically. Strain measurements on the sample's surface are used to gain information on the local behavior. The strain fields from simulations and experiments are compared for the validation of the modeled crack evolution.

This work aims to show the potential of the 3D elastic plastic non-local damage approach for wood. The non-local damage model is expanded from 2D to 3D and combined with physical information on the local fiber directions and plasticity for predicting the mechanical behavior of wood in different loading scenarios, wood species and wood qualities. Considering the computational challenges of the developed approach, the outcome of this study may be optimized in future for the strength prediction of the complex engineering systems, where local properties are important to be considered. It is possible to predict the mechanical behavior of the complex system with simplifications and the help of computer models.

Section ”Materials and methods” introduces the material and its properties based on the properties of clear wood samples and the local fiber orientation from laser scanning. It further summarizes the numerical method composed of non-local CDM for the brittle behavior under tension and orthotropic plasticity for the ductile behavior under compression. Three different validation examples are shown in Sect. ”Benchmark and problems: results and discussion”. Here, the conducted numerical results are validated against experimental data. The last complex application example presents an experimentally and numerically performed four-point bending test with specifically selected wooden imperfections in the area of constant moment.

Materials and methods

The objective is to develop a validated numerical model for strength prediction of timber boards with randomly distributed natural defects across various wood species. The developed method provides detailed information on the local strength and failure patterns of the samples, with the goal of e.g. contributing to the optimization of engineered wood products.

In order to achieve this, the numerical model presented in this contribution integrates material properties specific to the wood species and orthotropic direction (Sect. ”Mechanical and material properties”), the local orientation of the coordinate system along the samples and boards (Sects. ”Wooden imperfections in European beech boards, Representation of wooden imperfections in the model”), and the constitutive laws for wood (Sect. ”3D elastic plastic non-local CDM model”). This section details each of these three components respectively.

Mechanical and material properties

The mechanical and material properties of wood in this study are considered between meso and macro-scale and can be specified depending on the wood species. Mean values for the necessary material properties are taken from (uniaxial) tests on clear wood samples. Despite reducing the variation and size of the samples to small clear wood samples, still, the scatter of the material properties for this naturally grown material is considerable. Input values for the modeling process in this study are either taken from the database of Bollmus et al. (2022) or from the literature (Niemz and Sonderegger 2017; Akter et al. 2020; Seeber et al. 2024).

Depending on the specific directions, longitudinal, radial, and tangential, the elastic range and the post-elastic range, values are listed in Table 1 for the different wood species used in Sect. ”Benchmark and problems: results and discussion”.

Herein, benchmark and validation examples cover spruce (*Picea abies* L.), birch (*Betula pendula* Roth.), and European beech (*Fagus sylvatica* L.) and demonstrate the model’s applicability across various wood species. The first two benchmark examples in Sects. ”Benchmark example 1: tensile birch veneer tests and Benchmark example 2: spruce rolling shear tests” focus on verifying the method using clear wood samples. In contrast, the validation example in Sect. ”Validation example: four-point bending tests” examines board samples with more complex growth effects and local fiber deviation.

Wooden imperfections in European beech boards

European beech, and more generally hardwoods, exhibit complex growth patterns with fewer density variations compared to e.g. softwoods like spruce and they feature irregular inhomogeneities and fiber patterns (Frühwald and Schickhofer 2004; Rais et al. 2021). Such frequently and irregularly occurring imperfections can not be avoided, but are crucial for strength prediction and optimized engineered wood products such as e.g. glued laminated timber (GLT).

In Sect. ”Validation example: four-point bending tests”, selected European beech board samples of varying quality are investigated. The set of boards includes both low- and high-graded timber. The initial geometry of the boards was $2400 \times 90 \times 20\,\mathrm{mm}^3$, where the dynamic modulus of elasticity and the global density were measured. Laser scanning was performed to obtain the local direction of fibers on the four surfaces (Microtec, Bressanone, Italy). Two exemplary boards are visualized in Fig. 1a.

Table 1 Mechanical material properties of different wood species modeled in Sect. ”Benchmark and problems: results and discussion”

		Birch veneer	Spruce	European beech
		Bollmus et al. (2022)	Akter et al. (2020)	Seeber et al. (2024)
Elastic				
E_L	[MPa]	12,676	12,000	12,500
E_R		–	830	2050
E_T		213	545	810
G_{LR}		–	500	1640
G_{LT}		851	550	1080
G_{RT}		–	55	470
ν_{LR}	[–]	–	0.42	0.43
ν_{LT}		0.13	0.42	0.58
ν_{RT}		–	0.42	0.61
ν_{RL}		–	0.04	0.04
ν_{TL}		–	0.04	0.04
ν_{TR}		–	0.42	0.31
Post-elastic				
$f_{t,L}$	[MPa]	60.5	50	134
$f_{t,R}$		–	2.75	18
$f_{t,T}$		1.6	3.28	8
$f_{c,L}$		–	50	62
$f_{c,R}$		–	4.58	15.5
$f_{c,T}$		–	4.25	8
$f_{v,LR}$		–	1.54	14
$f_{v,LT}$		4.1	1.54	18
$f_{v,RT}$		–	1.54	15
Numerical				
α	[–]	0.99	0.99	0.99
β		1	[0.01, 10]	10
l_c	[mm]	0.1	[0.1, 1]	0.1
η		5	5	5
R		0.005	0.005	0.005
Q_i	[MPa]	–	$0.3{*}f_{c,i}$	$0.3{*}f_{c,i}$
b_i	[–]	–	2	2

For the validation of the numerical method in this contribution (Sect. ”Validation example: four-point bending tests”), test samples with dimensions of $l \times w \times t = 850 \times 80 \times 20\mathrm{mm}^3$ are selected from the database as visualized in Fig. 2. These test samples are selected based on different material growth defects influencing the strength and initiating failure. Herein, the material growth defect is positioned in the middle of the sample while in the remaining part of the sample, the local and global coordinate systems align together. Due to the mixture of quality of the available lamella set, test samples with different wooden growth defects influencing the strength of the material could be investigated systematically in Sect. ”Validation example: four-point bending tests”.

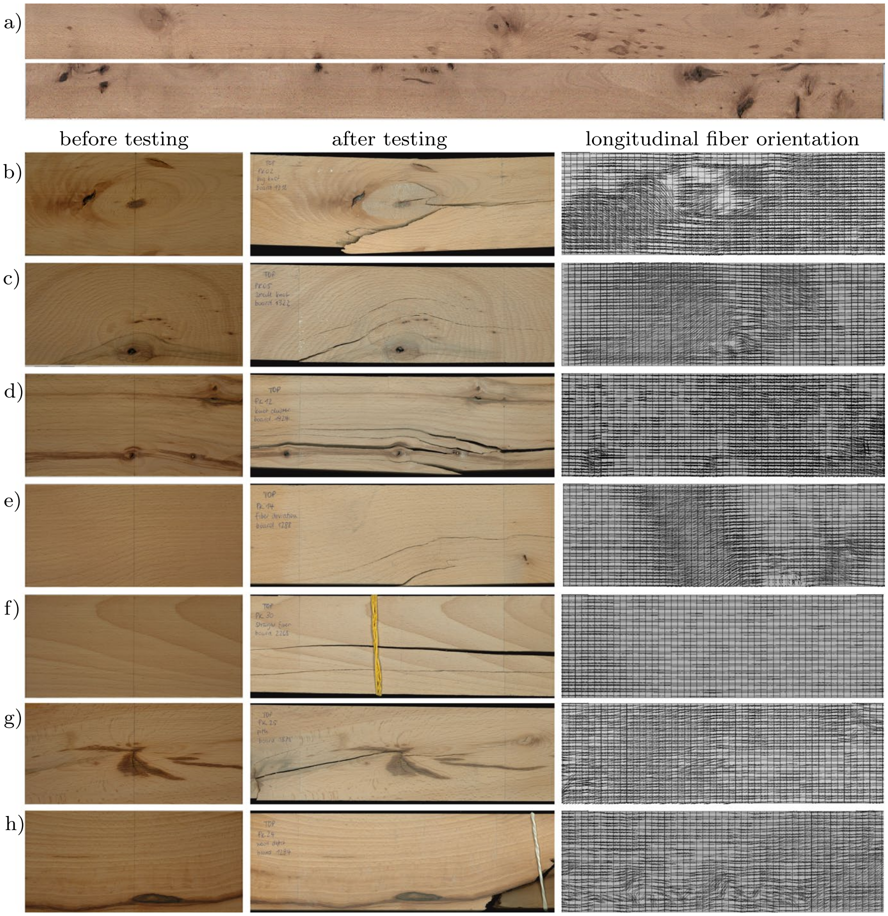

Fig. 1 Overview of European beech boards with heterogeneities: **a** shows exemplarily the top surface of two lamellas; **b**–**h** shows extracts of areas with different wooden imperfections (left), its representation through the local coordinate system in the FE-Model (right), and the failure in four-point bending (middle); **b** Single knot (Cat.1); **c** Single small knot (Cat.2); **d** Knot group (Cat.3); **e** Local fiber deviation (Cat.4); **f** Global straight fiber direction (Cat.5); **g** Pith push through (Cat.6); **h** Growth defect (Cat.7)

Natural material growth defects determining the strength of the board are generally called wooden imperfections and are classified into the seven categories in this study. These categories are classified by visual grading criteria and influence the strength of boards. The distinction of different categories (presented in Fig. 1) allows a systematic investigation of the different wooden imperfections and their influence on the strength and fracture pattern. Four samples are tested for each category and one exemplary image is shown in Fig. 1b–h on the left side.

1. Single knot: The knot is present through the whole thickness *t* of the board. It is located in the middle of the width of the board and has grown together with

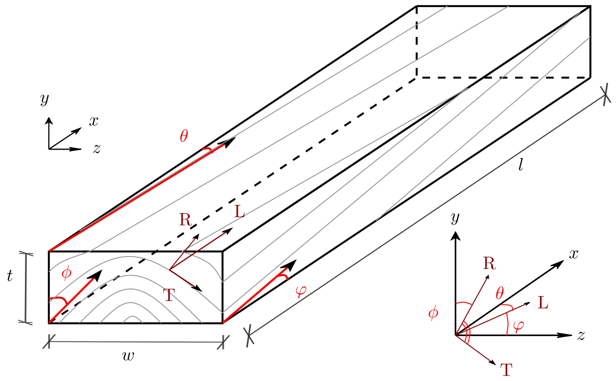

Fig. 2 Local coordinate system concerning the fiber direction (L, R, T), global board coordinate system (x, y, z), and the respective angles (θ, φ, ϕ) for the transformation between each other according to (Seeber et al. 2023)

its surroundings. The knot has a minimal diameter of $0.33 \times w$ and a maximal diameter of $0.5 \times w$.

2. Single small knot: The single small knot has a maximum diameter of $0.33 \times w$ and is not positioned in the middle of the board. The knot can be overgrown with the surroundings, can have different colors, or be a dead knot.
3. Knot cluster: The samples with a knot cluster contain a minimum of two and a maximum of five knots in the middle area of the test sample. Their diameter is restricted to be smaller than $0.33 \times w$.
4. Local fiber deviation: The area of fiber deviation is larger than $0.5 \times w$ and no knot is visible in the board sample. The cause of the fiber deviation might still be a knot, but not necessarily.
5. Global straight fiber direction: This group contains boards where the projection of the local longitudinal fiber orientation (L) and global board orientation (x) align with a max. deviation of 3°.
6. Pith push through: Pith variations occur frequently in hardwoods. Therefore, the effect of such imperfections on the strength of the board and the failure pattern is investigated in this category.
7. Growth defect: Wooden defects that are unrelated to a knot and often show a darker color are combined in this category. It can be ingrown bark or discolorations that might only influence the appearance of the material or can affect the strength.

Representation of wooden imperfections in the model

In the numerical model wooden imperfections described before are represented through the local coordinate system at each integration point.

By analyzing the laser scanning data of the four surfaces of boards the projection of the longitudinal fiber axis on the board surface is first depicted, via varying light scattering in the fiber direction and perpendicular to the fiber direction. The fiber orientation is included according to Seeber et al. (2023).

Additionally, as visualized in Fig. 3 the two end-grain surfaces of the test samples provide information on the position of the pith and consequently the radial and tangential direction inside the board. The position of the pith is detected on both end-grain surfaces of each board and the mean value is included in the model.

Subsequently, the interpolation of fiber orientation from surface data to the interior of the board is achieved through linear radial interpolation relative to the pith's position on a regular grid with a grid-point spacing of 2 mm.

For category 1, knots with a diameter larger than $0.33 \times w$ are clustered with the DBSCAN- and ConvexHull-algorithm from the common Python libraries sklearn, and scipy. The algorithms are fed with the information on fiber deviation and ellipse ratio from laser scanning. Knots, as clusters, are detected for a minimum size of $0.33 \times w$, defined by an amount of closely related points with a specific limiting fiber deviation larger than 65° and ellipse ratio (major axis/minor axis) smaller than 50. A convex hull is then built around the clustered knot and the local fiber coordinate system is defined with the longitudinal fiber direction in the thickness direction of the board, the radial and tangential direction in a circle around the center point of the knot perpendicular to the longitudinal fiber axis.

Since the density difference between a knot and clear wood is not significantly noticeable for beechwood, the same material properties are considered for both parts. Figure 1b–f shows the wooden imperfection of the board on the left, while the 2D local fiber orientation for the same imperfection is presented on the right. The middle shows the failure of the same board after testing in four-point bending, according to Sect. "Validation example: four-point bending tests".

Finally, the local fiber pattern in longitudinal, radial, and tangential directions is included in the model according to Seeber et al. (2023) by mapping and transforming the local fiber orientation to the local coordinate system of each integration point in the numerical model.

3D elastic plastic non-local CDM model

This section introduces the constitutive laws for wood as well as its numerical combination of based on the work presented in Seeber et al. (2024, 2025). Different material behaviors need to be distinguished for tension/shear and compression. While the ductile material behavior under compression is modeled with modified orthotropic Hill-plasticity and an exponential hardening law, the brittle material behavior in tension/shear is modeled with a sudden brittle damage model and accumulates to localized cracks represented with non-local damage until failure.

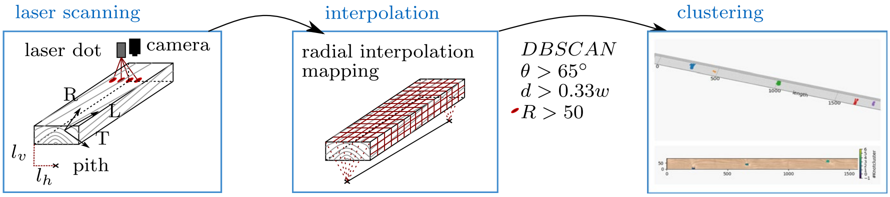

Fig. 3 Workflow for preparing the physical data for its inclusion in Abaqus as local fiber orientation

Local orthotropic continuum damage theory

The elastic range of the material is described by Hooke's law:

$$\begin{aligned} \hat{\boldsymbol{\sigma}} &= \mathrm{C}_0 \boldsymbol{\varepsilon}^{\mathrm{e}}, \\ \boldsymbol{\sigma} &= \mathrm{C}_{\mathrm{d}} \boldsymbol{\varepsilon}^{\mathrm{e}}. \end{aligned} \tag{1}$$

where $\hat{\boldsymbol{\sigma}}$ is the effective stress acting only on the elastic, non-damaged material according to CDM (Lemaître and Desmorat 2005) and C_0 is the initial elastic orthotropic stiffness tensor. The stress $\boldsymbol{\sigma}$ in a damaged state is computed using the elastic-damaging orthotropic stiffness tensor C_{d}. For this purpose, the strain vector $\boldsymbol{\varepsilon}$ is composed of an elastic part $\boldsymbol{\varepsilon}^{\mathrm{e}}$ and a plastic part $\boldsymbol{\varepsilon}^{\mathrm{p}}$:

$$\boldsymbol{\varepsilon} = \boldsymbol{\varepsilon}^{\mathrm{e}} + \boldsymbol{\varepsilon}^{\mathrm{p}}, \tag{2}$$

and the stress tensors can be computed as:

$$\begin{aligned} \hat{\boldsymbol{\sigma}} &= \mathrm{C}_0 (\boldsymbol{\varepsilon} - \boldsymbol{\varepsilon}^{\mathrm{p}}), \\ \boldsymbol{\sigma} &= \mathrm{C}_{\mathrm{d}} (\boldsymbol{\varepsilon} - \boldsymbol{\varepsilon}^{\mathrm{p}}). \end{aligned} \tag{3}$$

The Voigt notation is used to express the relevant entities and their relationships. Therefore, vectors $\boldsymbol{\varepsilon} = \{\varepsilon_{xx}, \varepsilon_{yy}, \varepsilon_{zz}, 2\varepsilon_{xy}, 2\varepsilon_{xz}, 2\varepsilon_{yz}\}^T$ and $\boldsymbol{\sigma} = \{\sigma_{xx}, \sigma_{yy}, \sigma_{xy}, \sigma_{xz}, \sigma_{yz}\}^T$ collect the six strain and stress components describing the equilibrium problem in the (x, y, z) plane. The six components are hereafter simplified by the index $i = [\mathrm{L}, \mathrm{R}, \mathrm{T}, \mathrm{LR}, \mathrm{LT}, \mathrm{RT}]$.

The end of the elastic range and the start of damage evolution are defined by the damage initiation criteria. Various criteria exist for wood commonly inspired by composites (Tsai and Wu 1971; Hashin 1980; Sandhaas et al. 2019). However, in this contribution, the separate damage mode criterion composed of the maximum stress criterion in the different directions is considered in tension/shear as,

$$\begin{aligned} &\tilde{\mathrm{s}}_{\mathrm{L}} = \frac{\hat{\sigma}_{11}}{f_{\mathrm{t,L}}}, \quad \tilde{\mathrm{s}}_{\mathrm{R}} = \frac{\hat{\sigma}_{22}}{f_{\mathrm{t,R}}}, \quad \tilde{\mathrm{s}}_{\mathrm{T}} = \frac{\hat{\sigma}_{33}}{f_{\mathrm{t,T}}}, \\ &\tilde{\mathrm{s}}_{\mathrm{LR}} = \frac{\hat{\sigma}_{12}}{f_{\mathrm{v,LR}}}, \quad \tilde{\mathrm{s}}_{\mathrm{LT}} = \frac{\hat{\sigma}_{13}}{f_{\mathrm{v,LT}}}, \quad \tilde{\mathrm{s}}_{\mathrm{RT}} = \frac{\hat{\sigma}_{23}}{f_{\mathrm{v,RT}}}, \end{aligned} \tag{4}$$

where the effective stress in tension/shear is compared to the strength in the consistent direction $f_{t/v,i}$ and expressed as damage initiation state variable $\tilde{s}_i$. Subsequently, damage evolves following the damage evolution law. In this contribution, the exponential damage evolution law (Peerlings et al. 1996) is used as

$$d_i(\kappa_i) = \begin{cases} 0 & \tilde{s}_i < \kappa_0 \\ 1 - \dfrac{\kappa_0}{\kappa_i}\left[1 - \alpha + \alpha \exp\left(-\beta(\kappa_i - \kappa_0)\right)\right] & \tilde{s}_i \geq \kappa_0, \end{cases} \tag{5}$$

where $\tilde{s}_i$ is the state variable defined in Eq. (4) based on the non-local stress in the corresponding direction $i = [\mathrm{L}, \mathrm{R}, \mathrm{T}, \mathrm{LR}, \mathrm{LT}, \mathrm{RT}]$, κ_i is the history parameter as $\kappa_i = \max\{1, \max(\mathrm{F}_i^{\mathrm{incr}})\}$, and κ_0 is defined as 1, implying that the stress has reached the specific strength. α represents the residual strength of the material when fully damaged and β defines the slope of the softening curve (Nguyen et al. 2018). Finally, the damage loading function for each stress field results in:

$$F_i(\tilde{s}_i, \kappa_i) = \tilde{s}_i - \kappa_i, \tag{6}$$

and the Kuhn-Tucker condition needs to be fulfilled as

$$\dot{\kappa}_i \geq 0, \quad \tilde{s}_i - \kappa_i \leq 0, \quad \dot{\kappa}_i(\tilde{s}_i - \kappa_i) = 0. \tag{7}$$

The second Kuhn-Tucker condition expresses the growth of damage variables and needs to be met as:

$$\dot{d}_i \geq 0. \tag{8}$$

Once the scalar damage variables are computed, the elastic-damaging orthotropic stiffness tensor $\mathrm{C_d}$ is computed as the inverse of the compliance matrix $\mathrm{C_d} = \mathrm{D_d^{-1}}$, the latter being defined as:

$$\mathrm{D_d} = \begin{bmatrix} \frac{1}{(1-\mathrm{d_L})\mathrm{E_{11}}} & \frac{-\nu_{21}}{\mathrm{E_{22}}} & \frac{-\nu_{31}}{\mathrm{E_{33}}} & 0 & 0 & 0 \\ \frac{-\nu_{12}}{\mathrm{E_{11}}} & \frac{1}{(1-\mathrm{d_R})\mathrm{E_{22}}} & \frac{-\nu_{32}}{\mathrm{E_{33}}} & 0 & 0 & 0 \\ \frac{-\nu_{13}}{\mathrm{E_{11}}} & \frac{-\nu_{23}}{\mathrm{E_{22}}} & \frac{1}{(1-\mathrm{d_T})\mathrm{E_{33}}} & 0 & 0 & 0 \\ 0 & 0 & 0 & \frac{1}{(1-\mathrm{d_{v,LR}})\mathrm{G_{12}}} & 0 & 0 \\ 0 & 0 & 0 & 0 & \frac{1}{(1-\mathrm{d_{v,LT}})\mathrm{G_{13}}} & 0 \\ 0 & 0 & 0 & 0 & 0 & \frac{1}{(1-\mathrm{d_{v,RT}})\mathrm{G_{23}}} \end{bmatrix}. \tag{9}$$

Matrix $\mathrm{C_d}$ is then replaced in Eq. (3).

Non-local orthotropic continuum damage theory

To overcome mesh dependency due to localizing strain during softening in CDM, non-local damage was first introduced by Pijaudier-Cabot and Bažant (1987) based on the equivalent strain. In Seeber et al. (2025) the principle of non-local damage was further developed depending on the orthotropic stress. In the integral formulation, each non-local stress component $\tilde{s}_i$ at the actual point x is calculated together with the weighted average over a certain reference volume:

$$\tilde{s}_i(\mathrm{x}) = \frac{1}{V_\mathrm{r}(\mathrm{x})} \int_V \alpha(\mathrm{x}, \mathrm{y}) s_i(\mathrm{y}) \mathrm{dy}, \qquad \text{with} \quad V_\mathrm{r}(\mathrm{x}) = \int_V \alpha(\mathrm{x}, \mathrm{y}) \mathrm{dy}, \tag{10}$$

where α represents the scalar-valued weight function and depends on the Euclidean distance $\|\mathrm{x}-\mathrm{y}\|$ between point x and y. In Peerlings et al. (1996) and Seeber et al. (2025), this formulation is further derived to an implicit gradient-enhanced stress-based non-local damage formulation with

$$\tilde{s}_i - c_i \nabla^2 \tilde{s}_i = s_i, \tag{11}$$

for computational efficiency. Consequently, Neumann boundary conditions

$$\nabla \tilde{s}_i \cdot \mathrm{n} = 0, \tag{12}$$

need to be fulfilled for each $\nabla \tilde{s}_i$, where n is the outward normal vector. The fracturing process of quasi-brittle materials typically starts as a diffusive network of micro-cracks and then localizes into a macro-crack, where the non-local interaction domain needs to be reduced drastically. This provides a physical motivation for introducing a localizing damage interaction function g_i. Following Geers et al. (1998), the characteristic length $c_i = l_{c,i}^2$ is replaced by the product of $g_i l_{c,i}^2$, so that Eq. (11) is replaced as:

$$s_i - \tilde{s}_i + \nabla(g_i l_{c,i}^2 \nabla \tilde{s}_i) = 0. \tag{13}$$

g_i is the localizing damage interaction function, which is equal to one during the elastic stage and takes the values of a residual interaction *R*, to be set close to zero, once the damage scalar $\tilde{d}_i$ reaches the unit value. For any other value of $\tilde{d}_i$, the exponential interaction function proposed by Poh and Sun (2017) is adopted, with η being a material constant:

$$g_i = \frac{(1-R)\exp(-\eta d_i) + R - \exp(-\eta)}{1-\exp(-\eta)}. \tag{14}$$

Plasticity

To consider the nonlinear orthotropic hardening behavior for wood, the Hill criterion is reformulated to Eq. (15) taking into account the orthotropic material character as presented in Seeber et al. (2024). The exponential isotropic hardening law $K(\alpha_j)$ from Voce (1948) with Q_j and b_j being the hardening parameters in the decisive direction *j* needs to be defined as:

$$\begin{aligned} f(\boldsymbol{\sigma},\alpha) &= \sqrt{\boldsymbol{\sigma}^{\mathrm{T}} : \tilde{\mathrm{A}} : \boldsymbol{\sigma}} - (f_{\mathrm{y},j} + K(\alpha_j)) \\ &= \sqrt{\boldsymbol{\sigma}^{\mathrm{T}} : \tilde{\mathrm{A}} : \boldsymbol{\sigma}} - (f_{\mathrm{y},j} + Q_j(1-e^{-b_j\alpha_j})). \end{aligned} \tag{15}$$

Herein, $f_{\mathrm{y},j}$ is the compressive yield strength in the decisive direction, and $\tilde{\mathrm{A}}$ is the modified orthotropic matrix of Hill-plasticity components following Seeber et al.

(2024). Consequently, the Kuhn-Tucker loading/unloading conditions need to be fulfilled:

$$\Delta\lambda \geq 0, \quad f(\boldsymbol{\sigma}, \alpha) \leq 0, \quad \Delta\lambda f(\boldsymbol{\sigma}, \alpha) = 0, \tag{16}$$

as well as the consistency conditions:

$$\Delta\lambda \dot{f}(\boldsymbol{\sigma}, \alpha) = 0, \quad \text{if} \quad f(\boldsymbol{\sigma}, \alpha) = 0. \tag{17}$$

Finally, the elastic plastic tangent modulus is expressed according to Simo and Ju (1989) as

$$\mathrm{C}_{\mathrm{ep}} = \begin{cases} \mathrm{C}_0 - \dfrac{\mathrm{C}_0 : \dfrac{\partial f}{\partial \boldsymbol{\sigma}} \otimes \mathrm{C}_0 : \dfrac{\partial f}{\partial \boldsymbol{\sigma}}}{\mathrm{C}_0 : \dfrac{\partial f}{\partial \boldsymbol{\sigma}} : \dfrac{\partial f}{\partial \boldsymbol{\sigma}} + \dfrac{\partial f}{\partial q} : \dfrac{\partial q}{\partial \alpha}} & \text{if } \Delta\lambda > 0 \\ \mathrm{C}_0 & \text{if } \Delta\lambda = 0. \end{cases} \tag{18}$$

Workflow and implementation

Simulations are performed in the commercial solver Abaqus and the implementation of the material laws is done in the form of user-defined subroutines (ORIENT/UMAT/UMATHT) in Abaqus.

In this contribution, the temperature variable θ and UMATHT are used for representing the additional non-local field and solving its PDE. Therefore, only one non-local variable can be used and needs to be defined in advance. Since the material strength of wood in the fiber direction is approximately a magnitude larger than in radial, tangential directions or shear strength, the material exhibits a high probability of failure in this direction. The naturally grown imperfections of different sizes in such material as well as the fiber deviations increase the possibility of failure in the weakest direction of the material, independent of the loading situation. Thus, the non-local driving failure is selected perpendicular to the fiber direction or in the shear direction for the examples in Sect. "Benchmark and problems: results and discussion", while the other damage parameters are kept as local parameters.

Detailed information about the implementation and workflow of the developed approach is described in Seeber et al. (2024, 2025).

Benchmark and problems: results and discussion

In this section, the non-local damage-plasticity model is applied to wood elements analysis and is validated on several benchmark examples, step by step increasing the complexity. Since the non-local CDM model was developed for 2D samples in Seeber et al. (2025), the first wooden validation example in Sect. "Benchmark example 1: tensile birch veneer tests" focuses on veneer samples with a 1 mm thickness, which can be simulated in 2D. Subsequently, Sect. "Benchmark example 2: spruce rolling shear tests" introduces a 3D example with brittle damage under rolling shear, which is validated based on the experimental data from the literature (Akter et al. 2020). The same example is loaded in compression in Sect. "Benchmark example 3: spruce compression tests" to validate the plasticity model. In the validation example, the investigation is extended beyond clear wood samples to analyze the fracture behavior in boards containing wooden imperfections. The test samples are loaded in four-point bending (Sect. "Validation example: four-point bending tests") and modeled utilizing the non-local CDM model. An overview of the numerical parameters of the non-local damage model for all benchmark examples is given in Table 2. The damage bandwidth $w_{\tilde{d}}$ is measured after the simulation and the smallest and largest damage bandwidth for the different benchmark examples are listed in the last column of the table. For all samples, the damage band spans over multiple elements but still does not spread over large parts of the samples and remains within the scope of a localized damage band due to the transient damage approach (Geers et al. 1998). Consequently, the damage band is always larger than the element size, even with the non-local lengths reported in Table 2 and shows the regularized non-local damage effect for all samples, similar to non-local damage results for fiber composites (Negi and Kumar 2019).

Benchmark example 1: tensile birch veneer tests

Since the non-local CDM model in Seeber et al. (2025) is developed and verified on two-dimensional benchmark examples for fiber-reinforced composites, birch veneers are chosen as first two-dimensional validation benchmark of the non-local CDM model on wood in this study. For this purpose, numerical results are compared to experimentally tested birch veneer samples with different global fiber orientations from (Bollmus et al. 2022).

Test setup

The test setup for both experimental and numerical tensile tests is shown in Fig. 4. For each direction with $\theta = [0^\circ, 15^\circ, 30^\circ, 60^\circ, 90^\circ]$, twenty (20) samples were tested

Table 2 Overview of the numerical parameters for non-local damage of the benchmark examples, where [min, max] of $w_{\tilde{d}}$ are the smallest and largest damage bandwidth of the decisive damage variable, measured after the simulation based on the damage profile results

Section	Test	h	t	w	el. size	l_c	β	[min, max] $w_{\tilde{d}}$
		[mm]	[mm]	[mm]	[mm]	[mm]	[−]	[mm]
Sect. "Benchmark example 1: tensile birch veneer tests"	Birch veneer	140	1	20	0.5	0.1	1	[1.5, 4.6]
Sect. "Benchmark example 2: spruce rolling shear tests"	Spruce rolling shear	40	10	50	[0.25, 1]	[0.1, 1]	[0.01, 10]	[2.4, 6.8]
Sect. "Benchmark example 3: spruce compression tests"	Spruce compression	40	10	50	1	–	–	–
Sect. "Validation example: four-point bending tests"	Beech four-pt-bend	80	20	750	2.5	0.1	10	[5.1, 17]

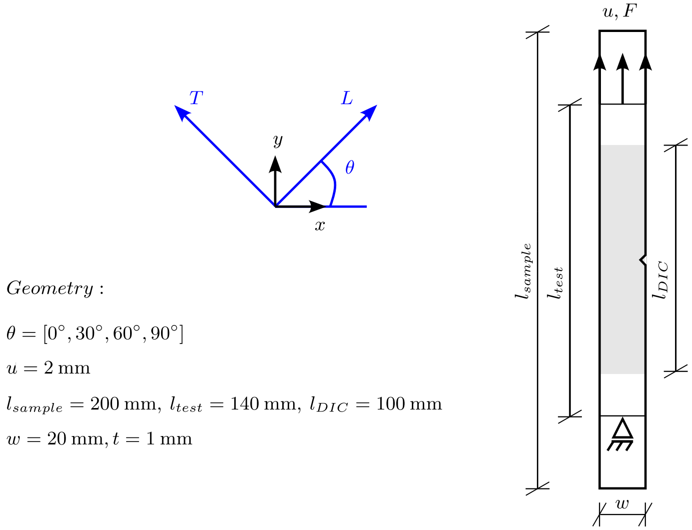

Fig. 4 Setup and geometry of the tensile tested veneer samples for experiments and simulation. The geometrical imperfection is only included in the numerical simulation, but not in the experimental tests

experimentally in Bollmus et al. (2022) and taken as validation data in this study. Before being experimentally tested, the samples were checked optically to exclude small fiber deviations. Still, the scatter in quality could not be fully excluded since wood is a naturally grown material. The samples were climatized at $20°\mathrm{C}$ and 65% RH and provided with a randomly sprayed pattern for optical strain measurement at the surface measurement area shown in Fig. 4. The tests from Bollmus et al. (2022) were performed displacement controlled at a strain rate of $1\%/\mathrm{min}$ with a universal testing machine and a load cell with a nominal load capacity of 5 kN. The strain in global directions x and y was measured in the area in the middle of the sample with the size of $100\,\mathrm{mm} \times w$.

Due to the minimal thickness of 1 mm, the numerical analysis has been performed in a plane stress state, and a geometrical imperfection has been added at the center of the sample edge in the y-direction to initiate the failure at this specific location. The mean values of material properties for birch veneer wood are taken from Bollmus et al. (2022) as material input properties. All the material properties are given in Table 1 and the parameters for damage evolution l_c, β-factor, are specified in Fig. 5. The boundary conditions are set according to Fig. 4. A clamped support is implemented on the bottom edge of the sample and the load is modeled as displacement-controlled on the top edge of the sample. An element size of 0.5 mm is found to be appropriate for a representative crack width, which ensures a good compromise between accuracy and computation effort. The non-local stress component governing the damage process leading to failure needs to be set in advance. For $\theta = [0°, 15°, 30°, 60°]$, the tangential stress $\tilde{\sigma}_{\mathrm{T}}$ is chosen to be non-local due its crucial role in crack initiation, while for $\theta = 90°$, the shear stress $\tilde{\sigma}_{\mathrm{LT}}$ is set non-local. Respectively $\tilde{d}_{\mathrm{T}}, \tilde{d}_{\mathrm{LT}}$ are evolving as visualized in Fig. 6.

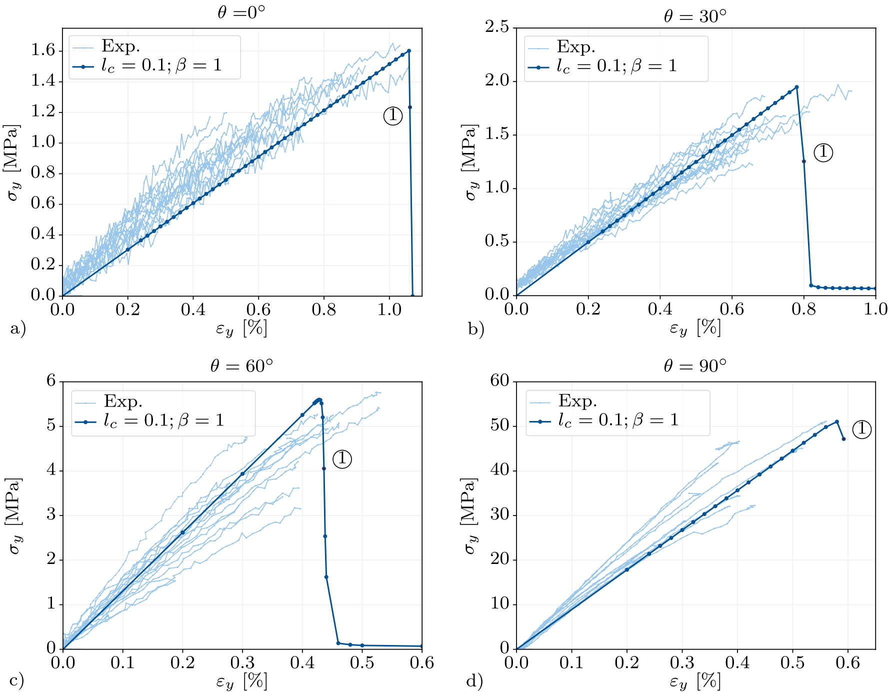

Fig. 5 Experimental and simulation results of the veneer test for four different orientations with $\theta = [0°, 30°, 60°, 90°]$ in **a**–**d** respectively. ① represents the time step of the numerical damage results visualized in Fig. 6

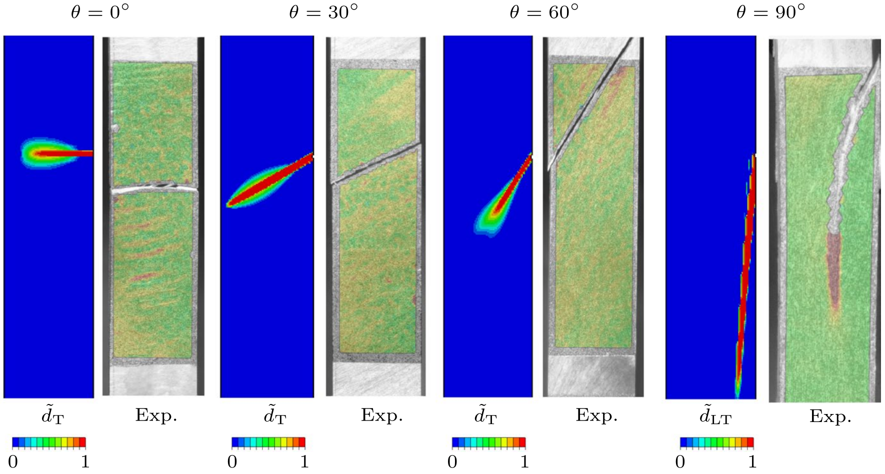

Fig. 6 Numerical damage results of the veneer test in different directions at time step ① shown in Fig. 5 compared to the respective experimental failure pattern

Experimental and simulation results

The experimental and numerical results are compared on the global structural level with stress–strain graphs in Fig. 5. The local failure pattern is investigated in Fig. 6. Since wood is a naturally grown fiber composite, a clear scatter can be observed in the graphs for thin veneer samples. It is shown in this figure that the simulation results represent the mechanical behavior of the material well. Experimental results show a slightly nonlinear behavior in the elastic material range which is not covered by the simulations. Nevertheless, the stiffness for all different orientations is correctly captured, as can be inferred from Fig. 5. Furthermore, an increasing load-carrying capacity is visible with increasing θ for both experimental and simulation results. The experiments could not capture the brittle material behavior after reaching the load-carrying capacity due to the high brittleness and the lack of a high-speed camera. The simulation, instead, is able to show the damaging process and the failure as well. Furthermore, the failure pattern has been investigated. The outcome of the investigation is exemplary shown in Fig. 6 at the time step ① marked in Fig. 5. It can be observed that for all directions the numerical damage pattern and damage direction agree well with the experimental fracture. The direction of damage propagation and its width, listed in Table 2 agrees with the experimental measurements. It shows a regularized damage band, which still represents the localized damage. In the experimental tests, the starting level of fracture varies due to inherent material heterogeneity and inevitable imperfections. In contrast, fracture initiates consistently at the geometric imperfection located at the center of the sample. In these examples, only the plotted damage variable evolves while the rest of the damage variables remain zero. For $\theta = [0^\circ, 30^\circ, 60^\circ]$, the stress in the tangential direction is selected as non-local stress $\tilde{s}_{\mathrm{T}}$, since this stress component is crucial for failure triggering in those cases. As shown in Fig. 6, the tangential damage variables evolve for the samples with the mentioned angles between $0^\circ - 60^\circ$. For $\theta = 90^\circ$ the fiber orientation in the numerical model is set to 89° to ease the damage initiation, as shown in Fig. 6, while the shear stress $\tilde{s}_{\mathrm{LT}}$ is treated as non-local. If a different direction would be represented non-locally, the model would behave like local CDM, because the non-local damage variable would not evolve. Consequently, damage would localize without reaching convergence directly after damage initiation.

Benchmark example 2: spruce rolling shear tests

To verify if the developed non-local CDM model can properly capture the brittle tensile/shear behavior of wood specimens, a second example is considered in this section. The benchmark exploits extensive experimental and numerical research on rolling shear tests carried out on spruce specimens, as documented in Akter et al. (2020, 2021). The results from the aforementioned studies are utilized as validation data in this section.

Test setup

The geometry, material properties, and experimental test results are taken from Akter et al. (2020, 2021) and are gathered in Table 1. The sample geometry is sketched in Fig. 7. Spruce samples are used for this set of tests. In this study, the simulated samples are oriented according to the rectangular coordinate system depicted in Fig. 7 representing a simplified approximation of reality. The boundary and loading conditions applied in the simulation are based on the numerical model presented in Akter et al. (2021), for comparison purposes. Loading is applied by controlling the displacement on the marked surfaces in Fig. 7. Similar to the experiments, a clamping volume with a thickness of 4 mm is considered in the simulation. Due to symmetry only half of the sample in the longitudinal direction has been modeled with prescribed symmetry boundary conditions according to Akter et al. (2021). The model is meshed with different mesh sizes dependent on the area of interest with higher/lower critical stresses/strains. Thus the middle part with the smallest and constant width is discretized with smaller elements varying between 0.25 mm and 5 mm. Based on convergence studies, an optimal element size of 1 mm is decided for the simulations.

Damage in the radial direction is processed non-locally while the other directions are kept local. This stress component is considered non-local in this benchmark case because it triggers the damage variable to evolve first. Characteristic length l_c and parameter β are varied and evaluated in a parametric study in the next section. Plasticity is not activated in this model, because shear/tensile stresses in the radial direction are increasing to a larger extent than compressive stresses in the radial direction. This benchmark example aims to model the failure mode with the brittle crack openings shown in Fig. 7b and neglects plasticity to analyze the performance of the non-local model separately.

Experimental and simulation results

The final experimental failure pattern is shown exemplarily for one sample in Fig. 7b. Force-displacement curves from the experiments, the curves from the simulation performed in Akter et al. (2021) with QMS-plasticity, as well as the ones from the current study are presented in Figs. 8, 9. as well as for the simulation performed.

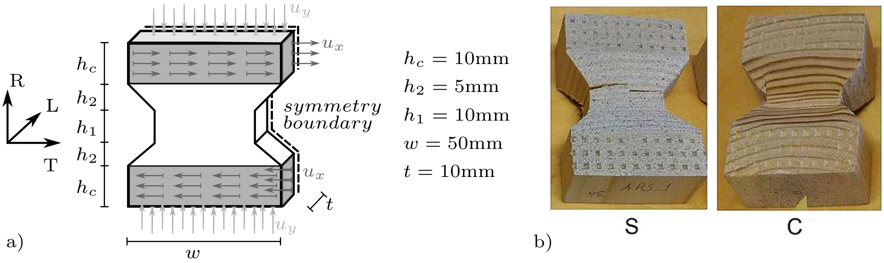

Fig. 7 **a** Geometry, material orientation, and testing setup of the experimental and numerical rolling shear test following Akter et al. (2020). **b** Failure mode of the samples in pure shear (S) with only u_x active and in compression (C) with only u_y active

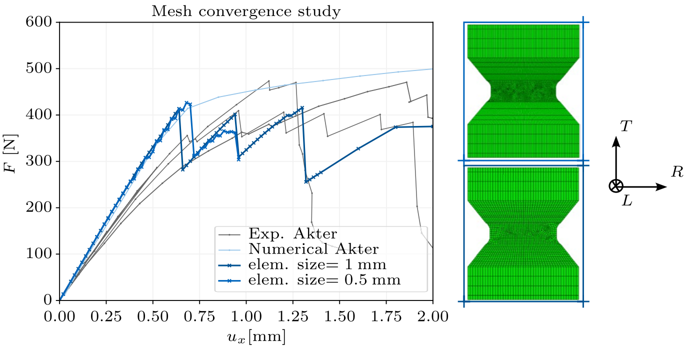

Fig. 8 Mesh convergence investigation for the radial shear test visualized for two different mesh sizes and compared to experimental and numerical data from Akter et al. (2021). Modeling parameters $l_c = 0.1$ and $\beta = 10$ are kept constant

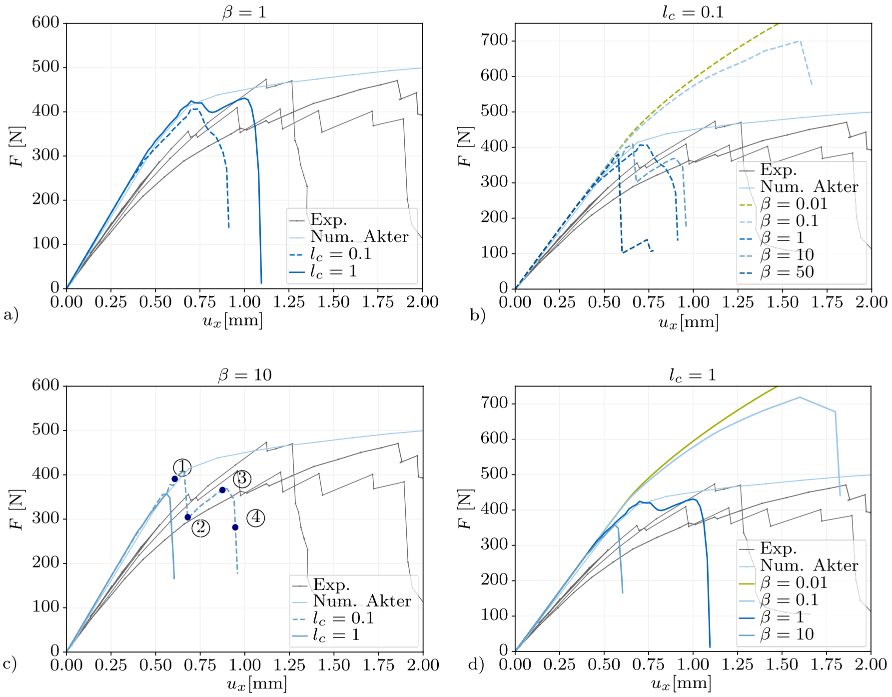

Fig. 9 Global force-displacement results for experimental and numerical radial shear tests. The sensitivity analysis on the modeling parameters is shown for tests with 1 mm element size. Four time steps are marked for the investigation of damage evolution in Fig. 10

Generally, the comparison of the experimental and numerical results shows satisfying accordance. The elastic stiffness of the non-local CDM model in this study matches the elastic stiffness reported in the numerical study by Akter et al. (2021), due to the identical material properties used. However, the experimental results exhibit slightly lower elastic stiffness. In the post-elastic range, elastic plastic models can be used to capture the nonlinear behavior (Akter et al. 2021). However, in the present contribution, non-local damage allows for simulation of the initial curvature in the force-displacement graph, as well as the exhibited force drops and the fracture pattern of the final failed sample shown in Fig. 10.

The first numerical study in this example is performed to gain information on mesh convergence and to detect the appropriate mesh size. Different mesh sizes have been investigated, they are shown in Fig. 8 keeping the same modeling parameters with $l_c = 0.1$ and $\beta = 10$. Differences of less than 10% are noticeable for the load-carrying capacity at damage initiation. Furthermore, the global force-displacement and damage pattern are mutually consistent, with negligible differences during damage evolution until failure. In comparison, mesh convergence is reached with 1 mm element size for the same example treated in the literature (Akter et al. 2021). Finally, a mesh with 1 mm element size is used for the simulations.

The second numerical study in this example is shown in Fig. 9 and reflects on the parameters for modeling the damage behavior: the characteristic length l_c, necessary for non-local damage and β, necessary for the damage evolution law. Both parameters have considerable influence on the damage initiation and the damage evolution. Smaller β results in a more ductile damaging behavior whereas higher β leads to a more brittle behavior with abrupt force drops and faster damage propagation. l_c instead influences more the damage initiation, whereby a smaller characteristic length initiates damage earlier as can be seen Fig. 9a. Since wood behaves strongly brittle under tension/shear and the damage path with $\beta = 10$ and $l_c = 0.1$ are selected for the most accurate representation of the experimental shear test. Both parameters are material dependent and additional studies focusing on the specification of these parameters are necessary. This analysis aims to show the feasibility of the methodology on wood. Specific tests for deriving the characteristic length from direction dependent material characteristics e.g. the fracture energy should be performed in future. The damage pattern for four different time steps, specified in Fig. 9, is visualized for this simulation in Fig. 10. Damage initiates first at the kink of the sample in radial direction with $\tilde{d}_{\mathrm{R}}$ (first line in Fig. 10), and results in the first non-linear

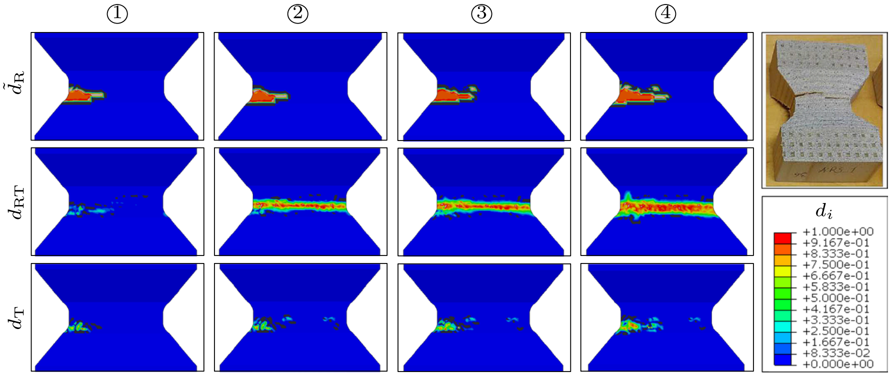

Fig. 10 Damage propagation of the relevant local and non-local damage variables for the numerical radial shear test at four different time steps marked in Fig. 9. The experimental failure pattern is visualized at the top right

curve in the force-displacement graph at time step ①. Damage then propagates with a minimum width of 2.4 mm and results in stress redistributions due to the reduced stiffness in the damaged elements. Stress redistributions further initiate damage in rolling shear d_{RT} along the whole width of the sample with a uniform shear stress along the whole width in global x-direction and narrow height in y-direction of the sample. This effect is also noticeable with the first drop in force in the global force-displacement graph at time step ②. Consequently, force starts to increase again ③ until a second radial crack propagates from the other side of the sample in tangential direction visualized. This finally leads to complete failure of the sample with the final drop in the force-displacement curve in time step ④.

In summary, the final failure pattern of the sample is in accordance with the experimentally failed sample shown on the right side in Fig. 10. The force-displacement results are covered satisfyingly. However, the model is still not capable of capturing the total amount of displacement/ductility as observed in the experiments.

Differentiation between failure modes is possible with this damage model and only one non-local damage variable is feasible to regularize the damage process for this example.

Benchmark example 3: spruce compression tests

For validating the plastic part of the elastic plastic non-local CDM model, the experimental results of the compression tests performed by Akter et al. (2020) are used for this third benchmark example.

Test setup

Regarding the geometry and the mesh, similar conditions as the previous benchmark case in Sect. ”Test setup” have been considered. Similarly, the same material, loading conditions (with $u_x = 0$), as shown in Fig. 7 in light grey color, have been used. An overall displacement of $u_y = 4$ mm is applied on the test sample in the radial direction and incremented through a displacement-controlled procedure. The global results of three experimental tests, as well as an exemplary strain measurement and the final deformed sample are available for this testing setup.

For the numerical simulation, the two modeling parameters for plasticity and the hardening law are set to $Q_i = 0.3 f_{c,i}$ and $b_i = 2$, respectively.

Experimental and simulation results

Global structural results in the form of force-displacement graphs and local strain measurements are visualized in Fig. 11a and b, respectively. The structural behavior of the simulation in this contribution is in good agreement with both the experimental and numerical results obtained through Akter et al.. QMS-plasticity model (Akter et al. 2021). The strain in y-direction at an exemplary time step ① is further visualized and shows strain pattern and size consistent with the experimental measurements as can be inferred from Fig. 11b.

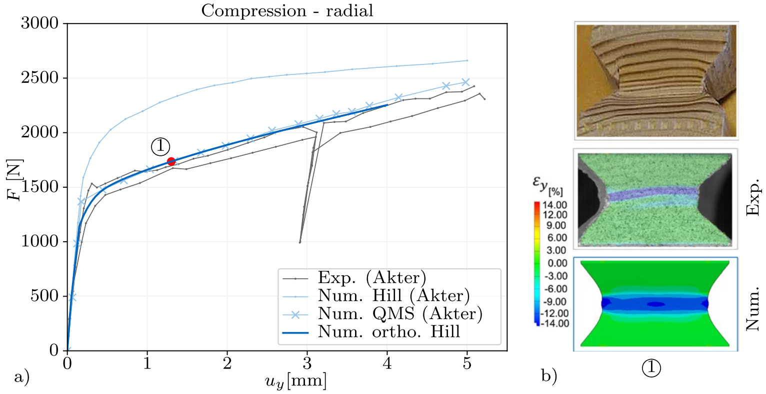

Fig. 11 Force-displacement results in (**a**) and the plastic strain pattern in y-direction in (**b**) of the numerical (ortho. Hill) and experimental (Akter et al. 2021) compression test at time step ①. The final deformed sample is shown at the top right

Although the numerical results are markedly influenced by the hardening parameters implemented as input data, the structural behavior under compression can be satisfactorily simulated with the proposed numerical model.

Validation example: four-point bending tests

In this section, the proposed non-local plastic CDM model is applied to a bending loading applied to the European beech boards with imperfections presented in Sect. ”Wooden imperfections in European beech boards”. The aim is to validate the developed numerical model regarding the capability of the model to capture complex crack patterns and their propagation in wood elements.

Within the framework of the activities carried out at Holzforschung München (HFM), experimental four-point bending tests were conducted on European beech boards featuring a selected wooden imperfection in the constant loading area. The advantage of this setup is to combine compression and tension in a single experiment. The testing configuration further avoids global shear forces in the critical area between the loading points effectively. Compared to a pure tensile test, this approach allows the use of a smaller load cell with a larger specimen cross-section, enabling a more extensive area for strain measurement and validation.

Experimental setup

The ratio of dimensions of the test samples was set according to the four-point bending test prescriptions in DIN 52186. The initial size of the boards, the possible space for the testing samples in the testing machine, and the size of the load cell needed to be considered. Consequently, the dimensions of the testing samples were set to $850 \times 80 \times 20\mathrm{mm}^3$. The geometrical and loading setup of the four-point bending test is visualized in Fig. 12, whereas the experimental setup is shown in Fig. 13. Load distribution plates of steel were used for the application of the load/displacement and

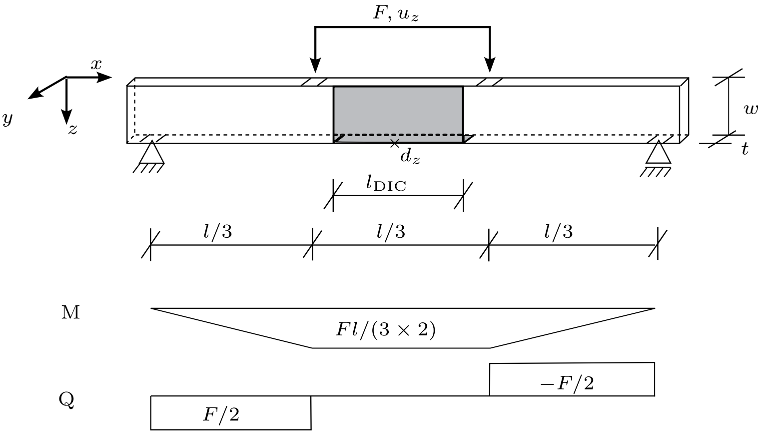

l, w, t = length, width, thickness of test sample = 750mm, 80mm, 20mm
l_{DIC} = length of strain measurement area
F = displacement(u_z) controlled force
M, Q = bending moment, shear force

Fig. 12 Geometrical and loading setup of the four-point bending test on wooden boards with a categorized imperfection in the marked strain measurement area. Shear force and bending moment diagrams are shown

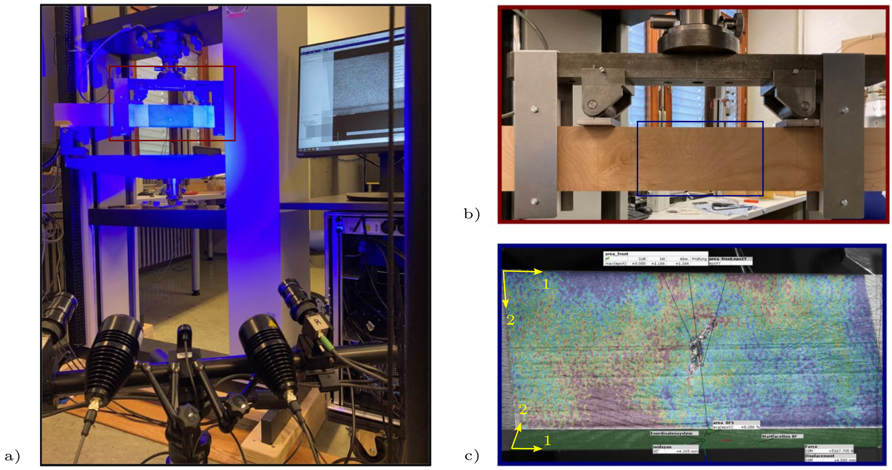

Fig. 13 The experimental setup of the four-point-bending-test experimental is shown with the camera system for strain measurement in (**a**). The zoom in (**b**) shows the test sample in the interested area of the constant moment without a sparkled pattern for the DIC measurement, tilting protections, and load-distribution plates. A second zoom-in (**c**) visualizes the detected strain measurement on the front and bottom sparkled surfaces in the GOM software during loading. The 2D coordinate system for the strain fields is shown

the bearings. A tilting protection was installed to prevent the samples from buckling for safety reasons but turned out to be not necessary for any tested sample.

Four test samples for each category, introduced in Sect. ”Materials and methods”, were climatized and tested at $20^\circ\mathrm{C}$ and 65% RH. The strain measurement area was located in the middle of the sample, concurring with the area of the wooden imperfection and the constant loading. The size of the measurement area was $l_{\mathrm{DIC}} \times w$ at the front and $l_{\mathrm{DIC}} \times t$ at the bottom surface. These surfaces of the test sample were covered with a random black/white dotted pattern to detect the strains with the DIC, visualized in Fig. 13. The tests were performed displacement-controlled with a loading speed of 3 mm/min until failure and the strains were detected with the camera system placed below the samples following the guidelines in the GOM-system (GOM GmbH, Braunschweig). Local strain in the global orientation (x, z) was detected on the front and in orientation (x, y) bottom surface. Moreover, force and displacement were recorded by the machine, and the displacement in the z-direction at the middle point (Fig. 12) of the sample d_z was stored separately from the DIC data. The optical system depicted the crack pattern in the recorded area. However, the way of brittle crack propagation could only be detected for the final crack propagation step or slow-growing cracks because standard cameras were used in this study. For the detection of more steps during crack propagation, high-speed cameras would be necessary.

The failure pattern was dominated by the wooden imperfection and different crack patterns were detected. They are analyzed in Sect. “Four-point-bending test results” and can be visualized in Fig. 1 on the right. Fracture initiated in the middle area of constant loading for all categories of boards mentioned in Sect. ”Wooden imperfections in European beech boards”, apart from Cat. 5 with the global straight fiber orientation. In contrast, boards of this category mainly failed due to shear outside of the DIC measurement area.

Numerical setup

The geometry and boundary conditions for the numerical simulations are visualized in Fig. 12 and the material properties are listed in Table 1. For the full four-point bending test, the boundary conditions are induced with rigid bodies at the load-inducing areas. A negative displacement of $15\mathrm{mm}$ is applied by the top rigid bodies with steps of size 0.01 mm. Hard contact in z-direction and a friction coefficient of 0.1 in x- and y-direction define the contact.

A second model was set up for the analysis of the crack pattern, where only the center part of the test in the area between the load-inducing points is modeled. The rotation around the global y-axis (Fig. 12) has been introduced in the middle ($w/2$) of the two sides of this simplified sample, while the displacement/rotation in the other directions are fixed. For this model, a finer discretization has been considered and the crack propagation has been investigated in more detail.

The discretization of the full model is set to elements of 20 mm in length at the left and right sides and 5 mm in the middle area between the loading points. The simplified model instead is discretized with a uniform mesh of 2.5 mm. This latter mesh size is chosen according to a performed mesh convergence study in the elastic range. The stress in the tangential direction is selected as the non-local criterion governing damage evolution, corresponding to $\tilde{\sigma}_{\mathrm{T}}$ and $\tilde{d}_{\mathrm{T}}$, because mostly cracks are propagating in the LR-plane and are thus probably triggered by tension in the tangential direction. Parameters for the non-local CDM method have been set to $l_c = 0.1$ and $\beta = 10$ in all models. To verify the methodology systematically, no plasticity is included in the simulation of the four-point bending tests with wooden imperfections. This simplification can only be done for boards with an early strongly brittle material behavior. Especially for Cat. 5 with global straight fiber orientation this simplification is no longer valid.

The local coordinate system at each integration point is introduced using the laser scanning information and the Abaqus-subroutine ORIENT according to Seeber et al. (2023). Integration points have been deleted when one of the six damage variables reaches the value one. This describes the physical crack opening and leads to a better convergence while neglecting high deformations of elements with reduced damaged stiffness.

Four-point-bending test results

Prediction of the brittle fracture behavior of wooden boards with imperfections is complex and requires a correct representation of the elastic and post-elastic material behavior including material input parameters and constitutive laws. This specifically raises the following question:

Can the fracture of wood with complex natural growth be described by the numerical model with local fiber deviations and homogenized clear wood material parameters? To specifically answer this question, simulations are performed with the non-local CDM and compared to experimental results of the test samples from different categories described in Sect. ”Experimental setup”. Three exemplary test samples are visualized and discussed in the following paragraphs. Test sample PK4 from category 1, representing boards with a single knot, test sample PK5 from category 2, representing boards with a single small knot, shown in Fig. 1b, and test sample PK14 from category 4 representing boards with fiber deviation. Test specimen PK5 is described in detail in the following paragraphs. Subsequently, a discussion regarding samples with the different heterogeneities is given by showing the results of PK4 and PK14.

Global structural results are validated with force-displacement results investigating the load-carrying capacity. Moreover, local surface strains and crack patterns have been investigated for the validation of the elastic and post-elastic material behavior at different time steps in the marked measured area in the middle of the test sample.

The respective force-displacement curves for PK5 are shown in Fig. 14,left for the full model and compared to experimental results. Instead, for the simplified model, where the rotation around the y-axis is applied on both sides of the simplified modeled sample, the force-time graph is shown in Fig. 14,right and validated by experimental results. While in the full model, the drop in force at first damage initiation goes to zero without residual strength of the board, in the simplified model the drop in force is smaller and additional energy is applied until final failure of the model. The reason for this different global structural behavior might be related to the implementation of different boundary conditions for both models.

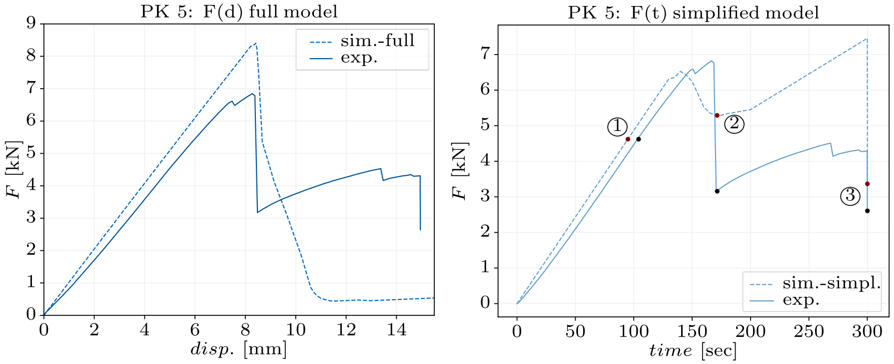

Fig. 14 Structural force-displacement results of test sample 5 from experiment and simulation

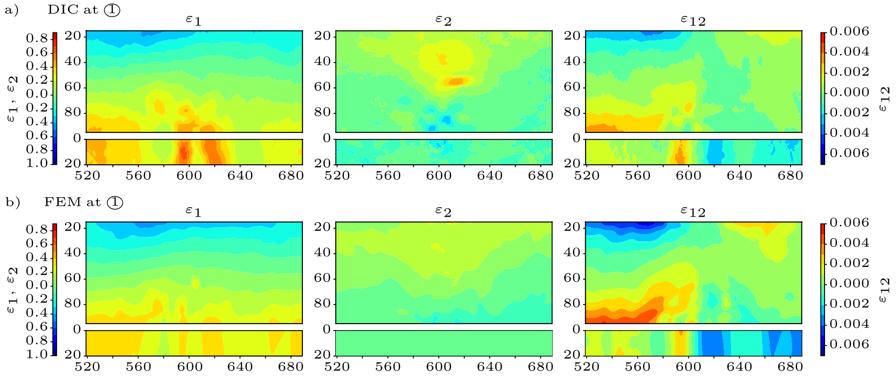

Fig. 15 The comparison of the global strains $\varepsilon_1, \varepsilon_2, \varepsilon_{12}$ is shown for the experimental strain fields (DIC) and the strain fields from simulation (FEM) at the specific time point ① in the elastic material range of PK5. Only the strains on the measured surface (specific dimensions in [mm]) are shown in the 2D coordinate systems from Fig. 13

Different time steps in Fig. 14, presented as ①,②, and ③, visualize the local material response on the surface of the simplified sample. The steps presented in the elastic range ① in Fig. 15, at the first propagated crack ② in Fig. 16 and at final failure ③ in Fig 17, where the experimental crack and numerical damage are visualized. These strain plots show the front and bottom surface of the test sample for the experimental results in (a) and the numerical results in (b). The experimental global strain in longitudinal board direction (ε_1) is visualized on the left side, the strain in y- or z-direction of the board (ε_2) in the middle of the figures and the global shear strain (ε_{12}) on the right side of the figures. The numerical strain with the same order and in the same global board directions is visualized in (b). The dimensions of the measured front and bottom areas are given in [mm] and the coordinate systems of the strain fields are visualized in Fig. 13.

Both, full and simplified models represent a slightly higher elastic stiffness than in the experiment (see Fig. 14). The reason for this might be the mean material input parameters for the elastic material behavior such as E_i, G_i. Also the comparison of

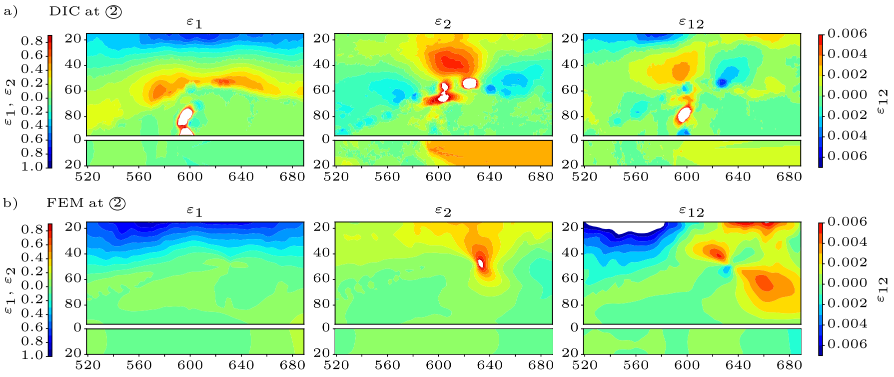

Fig. 16 The comparison of the global strains $\varepsilon_1, \varepsilon_2, \varepsilon_{12}$ is shown for the experimental strain fields (DIC) and the strain fields from simulation (FEM) at the specific time point ② at damage initiation of PK5. Only the strains on the measured surface (specific dimensions in [mm]) are shown in the 2D coordinate systems from Fig. 13

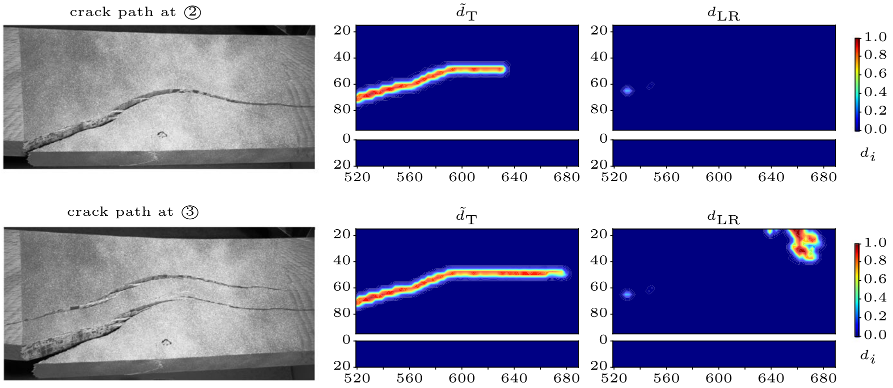

Fig. 17 Crack paths at the time steps ① and ② from the experiment (left) and damage path from the simulation (right)

the strain in Fig. 15, which depicts the strain in the elastic range at the first time step ①, reflects the stiffer behavior of the numerical model comparing the strain in the longitudinal board direction (left side). Nevertheless, the global strain pattern for both experimental and numerical results correspond well in all directions.

The second time step ② depicts the material behavior of the sample in the damaged range, where the first crack has initiated and propagated. While damage in the numerical model evolves less brittle, a strongly brittle crack propagates in the experiment at this time step as visualized in Fig. 14. The experimental crack path and the numerical damage paths at this stage are visualized in Fig. 17a. In the simulation, damage $\tilde{d}_T$ is triggered by the stress in the tangential direction and it propagates in the LR-plane similar to the crack in the experiment, which is propagating in the LR-plane as well. The location of damage initiation corresponds in both experiments and simulations, although in the simulation the crack propagates approximately 10 mm higher in y-direction. The crack band width is narrow, but spans over more than one element and can thus represent the thin localized crack in the experiment. While the damage variables in longitudinal fiber direction and radial direction remain zero, d_{LR} develops at the bottom edge ($x = 491$ mm) of the sample together with $\tilde{d}_{\mathrm{T}}$ and initiates out of the visualized strain measurement area.

The experimental and numerical strain fields are investigated at this stage in Fig. 16 as well. The numerical strain in the longitudinal board direction is slightly underestimated right above the crack, similar to the elastic range. Instead, the strain in the width direction and the shear strain show similar magnitude and pattern, as the experiments. The reason for this might be the underestimation of the complete crack propagation path in the simulations compared to the experiments as shown in Fig. 17. Instead, overestimation is visible in the shear strain on the right side.

The last time step ③ depicts the final failure of the sample, visualized in Fig. 17b. In the experiment, a second crack propagates parallel to the first crack and initiates due to shear stress at $x = 620$ mm. This second damage path does not evolve in the numerical model, but shear damage develops at $x = 660$ mm and leads to the final failure of the test.

The deletion of integration points, when the damage variable reaches the value one, represents the discontinuity in the model without evolving damage in the longitudinal fiber direction. Therefore, the model has a capacity for improvement in this direction.

It is shown, that damage is mainly triggered by the stress in the tangential direction. Similarly, the damage variable $\tilde{d}_{\mathrm{T}}$ in simulations initiates at the correct location ($x = 500$ mm) and evolves in the correct direction. At the same time, the shear damage variable d_{LR} initiates in the region of damage initiation ($x = 500$ mm). In the experiment, this is seen in form of a major kink formed by crushing cells. The final failure of the test sample is caused by a mixture of damage in the tangential direction and damage in the shear. Consequently, it can be described as a mixed failure mode. The global structural results predicting the maximum load-carrying capacity of the sample are slightly overestimated, probably due to the elastic material input parameters. However, these mean material input parameters could be adapted for the specific board, which is although not the purpose of this study.

Fig. 18 Structural results of test sample PK 4 from experiment and simulation

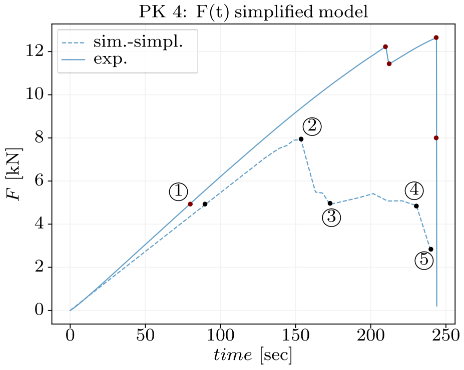

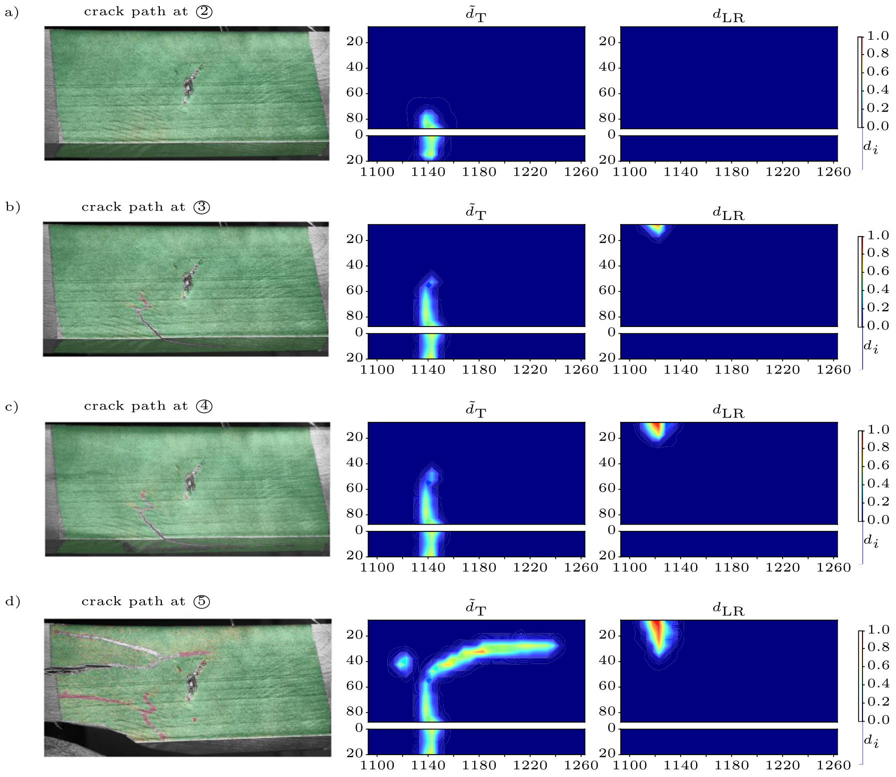

Fig. 19 Crack paths of PK 4 at the time steps ②–⑤ from the experiment (left) and damage path from the simulation (right)

Fig. 20 Structural results of test sample PK 14 from experiment and simulation

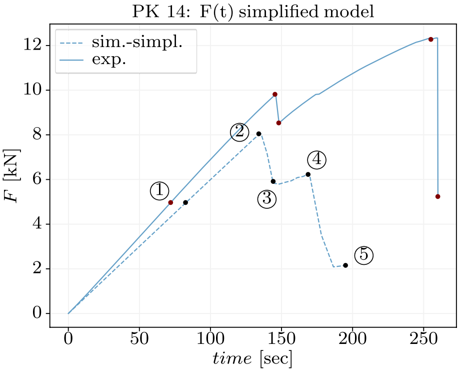

A comparison between experimental and numerical results for test samples with a single knot and a test sample with only fiber deviation is shown in Figs. 18, 19, 20, 21.

In contrast to the previously discussed test specimen PK5, the stiffness of PK4 and PK14 is slightly underestimated in the numerical analysis compared to its experimental test, shown in Figs. 18, 20. The reason might be the natural scatter of the material

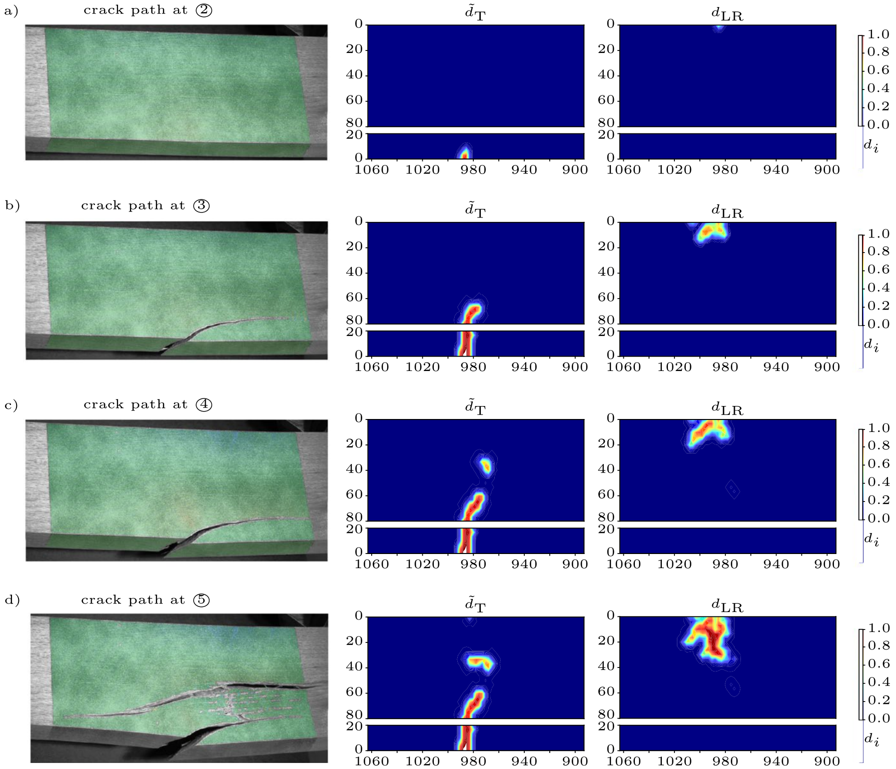

Fig. 21 Crack paths of PK 14 at the time steps ②–⑤ from the experiment (left) and damage path from the simulation (right)

input properties of wood, which are considered by the mean value in each direction. The numerical models of both samples do not reach the experimental peak force. The damage evolution law is decisive for influencing the damage propagation of micro-cracks and thus controlling the propagation speed of the macro-crack and global maximum force. In this study, a commonly known damage evolution law, introduced by Peerlings et al. (1996), was used to systematically validate the method. In future, for considering an accurate speed of micro-crack accumulation, this law could be replaced with a more appropriate law that takes into account material parameters of the compression mechanics of wood and thus also reflects the global load-deformation curve of the experiment.

Besides the global structural response of both test samples, the local results show the damage propagation process and are visualized in Figs. 19, 21. Four decisive steps in time are picked to compare the evolving damage during the experiment. For both test specimens, the failure parameter in the tangential direction is decisive, as the tangential strength is reached first with strong fiber deviation around the knot at the lower end of the board. The position and direction of the failure propagation of the simulation agrees well with the experimental results and the failure mode can thus be validated. All three test cases show that damage in tangential direction due to fiber deviation is decisive for damage initiation. Not just the knot, independent of its size, but rather the fiber deviation around the knot is decisive for failure initiation. Finally, shear strength in the LR plane is reached and the global failure of the sample can be described as an interaction of different failure modes shown with the different evolving damage variables.

These examples show us that a better understanding of the failure behavior of wood with imperfections can be gained with this method. An accurate representation of the mechanical behavior of wood is strongly dependent on material input parameters, 2D laser scanning information on the fiber orientation, numerical representation of the boundary conditions, and computational burden. Comparisons between different categories of wooden imperfections can show the amount of impact of different growth effects, especially local fiber deviation, on the strength of the material.

Conclusion and outlook

In this contribution, the 3D orthotropic elastic plastic non-local CDM developed by the authors is validated on different examples with increasing complexity. The method is independent of wood species and is validated on spruce, birch, and European beech. Further, the linear and non-linear as well as ductile and brittle material behavior of wood under shear loading is modeled and validated with experimental results from the literature. An interaction between different failure modes is assumed and presented in this study, although separate damage modes are treated differently here. Generally, this method provides valuable insights into the mixed-mode fracture of wood due to the separate treatment of damage variables in the orthotropic directions. The separate damage criteria in different directions can evolve simultaneously and represent the interaction of these damage variables. Consequently, this facilitates the analysis of mixed-mode failure patterns in wood.

Generally, all examples present a congruent material behavior with a qualitative and quantitative good agreement between experimental and numerical results. Crack initiation and crack propagation are captured well with the correct damage location, damage mode (variable), and damage propagation direction. The resulting strain pattern matches the experimentally measured strain on the surface, especially for the elastic range and damage initiation. While the crack propagation in the longitudinal direction is limited in the numerical approach, longer cracks in the x-direction are evolving in the experiments.

In comparison to the local CDM approach, the non-local CDM model does not localize damage in one element, but damage evolves across elements. One non-local variable shows regularized results in several directions. However, the non-local damage direction needs to be selected in advance, which can be difficult in complex models. Thus, further investigations with several non-local damage variables are needed to examine the model behavior. The examples in this contribution show a successful application of the 3D orthotropic elastic plastic non-local CDM model on wood. However, future investigations need to be done concerning the model/material parameters such as the characteristic length and the parameters for the exponential damage evolution law for wood. Moreover, several aspects such as various failure criteria, the amount of non-local damage variables, variations in boundary conditions, and the relation of the modeling parameters to the fracture toughness of wood are discussed in this contribution. To further improve the method, multiple non-local damage variables should be introduced. This is still a limiting factor on account of the implementation in the commercial solver Abaqus, which uses the temperature variable as a non-local field variable. Nevertheless, one decisive damage variable is emerging according to experience, while modeling all boards with different imperfections. As a next step, more experimental and numerical analysis on different wood species is needed to relate the modeling parameters l_c, α, β for non-local damage evolution to the material parameters like fracture energy or damage/crack width of wood dependent on the exact species.

It is difficult to impossible to fully reduce the uncertainty of the model due to the scatter of the material parameters of wood. This model simplifies the naturally grown heterogeneous material as homogeneous material additionally including local fiber orientation in each integration point of the model. Enhancement of the computational burden for solving the non-local field should be considered e.g. by including algorithms to compute the PDE of the non-local field independently. For improving strength prediction, higher resolution of the laser scanning data for the fiber orientation or even 3D data using CT-scanning could reduce uncertainties and would be beneficial for accuracy.

Acknowledgements The authors are grateful for the help of the wood science group of TUM, especially Max Engelhardt and Thomas Böger, during the experimental testing of the four-point bending tests. Moreover, the authors thank Microtec for the laser scanning data and the German Research Foundation (DFG) through TUM International Graduate School of Science and Engineering (IGSSE), GSC81 for the funding of the project “FaiMONat-Multi-fidelity Failure Modeling and Optimization for natural Fiber Structures in Complex Environments”.

Author contributions F.S.: Conceptualization, Methodology, Investigation, Data curation, Visualization, Writing-original draft; A.K.S.: Supervision, Funding acquisition, Writing—review & editing, Conceptualization; E.B.: Methodology, Investigation, Supervision, Writing—review & editing, Conceptualization; J.W.vdK.: Supervision, Resources, funding acquisition, Conceptualization.

Funding Open Access funding enabled and organized by Projekt DEAL.

Data availability No datasets were generated or analysed during the current study.

Declarations

Conflict of interest The authors declare no conflict of interest.

References

Akter S, Serrano E, Bader T (2020) Experimental assessment of failure criteria for the interaction of normal stress perpendicular to the grain with rolling shear stress in Norway spruce clear wood. Eur J Wood Prod 78:1105–1123. https://doi.org/10.1007/s00107-020-01587-w

Akter S, Serrano E, Bader T (2021) Numerical modelling of wood under combined loading of compression perpendicular to the grain and rolling shear. Eng Struct 244:112800. https://doi.org/10.1016/j.engstruct.2021.112800

Ambati M, Gerasimov T, De Lorenzis L (2014) A review on phase-field models of brittle fracture and a new fast hybrid formulation. Comput Mech 55:383. https://doi.org/10.1007/s00466-014-1109-y

Benvenuti E, Orlando N (2021) A mesh-independent framework for crack tracking in elastodamaging materials through the regularized extended finite element method. Comput Mech 68:25–49. https://doi.org/10.1007/s00466-021-02016-2

Benvenuti E, Orlando N, Gebhardt C et al (2020) An orthotropic multi-surface damage-plasticity FE-formulation for wood: part I–constitutive model. Comput Struct 240:106350. https://doi.org/10.1016/j.compstruc.2020.106350

Bollmus S, Buchelt B, Deetz R, et al (2022) Schlussbericht Verbundvorhaben: Holzbasierte Werkstoffe im Maschinenbau (HoMaba)–Berechnungskonzepte, Kennwertanforderungen, Kennwertermittlung [Final report of research collaboration: wood-based materials in mechanical engineering (HoMaba)–computational concepts, parameter requirements, determination of material properties]. https://doi.org/10.2314/KXP:1854984594

Danielsson H, Gustafsson PJ (2016) Fracture analysis of perpendicular to grain loaded dowel-type connections using a 3D cohesive zone model. Wood Mater Sci Eng 11(5):261–273. https://doi.org/10.1080/17480272.2014.982341

Francfort G, Marigo JJ (1998) Revisiting brittle fracture as an energy minimization problem. J Mech Phys Solids 46(8):1319–1342. https://doi.org/10.1016/S0022-5096(98)00034-9

Frühwald K, Schickhofer G (2004) Strength grading of hardwoods. In: 8th world conference on timber engineering, WCTE 2004, pp 675–679

Geers M, de Borst R, Brekelmans W et al (1998) Strain-based transient-gradient damage model for failure analyses. Comput Methods Appl Mech Eng 160(1):133–153. https://doi.org/10.1016/S0045-7825(98)80011-X

Hashin Z (1980) (1980) Failure criteria for unidirectional fiber composites. J Appl Mech 47:329–334

Khaloian Sarnaghi A, van de Kuilen JWG (2019) Strength prediction of timber boards using 3D FE-analysis. Constr Build Mater 202:563–573. https://doi.org/10.1016/j.conbuildmat.2019.01.032

Lemaître J, Desmorat R (2005) Engineering damage mechanics: Ductile, creep, fatigue and brittle failures. Springer, Berlin and New York

Lukacevic M, Füssl J, Lampert R (2015) Failure mechanisms of clear wood identified at wood cell level by an approach based on the extended finite element method. Eng Fract Mech 144:158–175. https://doi.org/10.1016/j.engfracmech.2015.06.066

Lukacevic M, Kandler G, Hu M et al (2019) A 3D model for knots and related fiber deviations in sawn timber for prediction of mechanical properties of boards. Mater Des 166:107617. https://doi.org/10.1016/j.matdes.2019.107617

Moës N, Belytschko T (2002) Extended finite element method for cohesive crack growth. Eng Fract Mech 69(7):813–833. https://doi.org/10.1016/S0013-7944(01)00128-X

Negi A, Kumar S (2019) Localizing gradient damage model with smoothed stress based anisotropic nonlocal interactions. Eng Fract Mech 214:21–39. https://doi.org/10.1016/j.engfracmech.2019.04.011

Nguyen T, Bui T, Hirose S (2018) Smoothing gradient damage model with evolving anisotropic nonlocal interactions tailored to low-order finite elements. Comput Methods Appl Mech Eng 328:498–541. https://doi.org/10.1016/j.cma.2017.09.019

Niemz P, Sonderegger WU (2017) Holzphysik: Physik des Holzes und der Holzwerkstoffe [Wood physics: physics of wood and wood-based materials]. Fachbuchverlag Leipzig Carl Hanser Verlag München. https://doi.org/10.3139/9783446445468

Ortiz M, Pandolfi A (1999) Finite-deformation irreversible cohesive elements for three-dimensional crack-propagation analysis. Int J Numer Meth Eng 44(9):1267–1282. https://doi.org/10.1002/(SICI)1097-0207(19990330)44:9%3C1267::AID-NME486%3E3.0.CO;2-7

Pantidis P, Mobasher ME (2023) Integrated finite element neural network (I-FENN) for non-local continuum damage mechanics. Comput Methods Appl Mech Eng 404:115766. https://doi.org/10.1016/j.cma.2022.115766

Pech S, Lukacevic M, Füssl J (2022) A hybrid multi-phase field model to describe cohesive failure in orthotropic materials, assessed by modeling failure mechanisms in wood. Eng Fract Mech 271:108591. https://doi.org/10.1016/j.engfracmech.2022.108591

Peerlings R, de Borst, R, Brekelmans W et al (1996) Gradient enhanced damage for quasi-brittle materials. Int J Numer Meth Eng 39(19):3391–3403. https://doi.org/10.1002/(SICI)1097-0207(19961015)39:19%3C3391::AID-NME7%3E3.0.CO;2-D

Pijaudier-Cabot G, Bažant ZP (1987) Nonlocal damage theory. J Eng Mech 113(10):1512–1533. https://doi.org/10.1061/(ASCE)0733-9399(1987)113:10(1512)

Poh L, Sun G (2017) Localizing gradient damage model with decreasing interactions. Int J Numer Meth Eng 110:503–522. https://doi.org/10.1002/nme.5364

Rais A, Bacher M, Khaloian-Sarnaghi A et al (2021) Local 3D fibre orientation for tensile strength prediction of European beech timber. Constr Build Mater 279:122527. https://doi.org/10.1016/j.conbuildmat.2021.122527

Resch E, Kaliske M (2010) Three-dimensional numerical analyses of load-bearing behavior and failure of multiple double-shear dowel-type connections in timber engineering. Comput Struct 88(3–4):165–177. https://doi.org/10.1016/j.compstruc.2009.09.002

Sandhaas C (2012) Mechanical behaviour of timber joints with slotted-in steel plates. Technische Universitet Delft, Delft

Sandhaas C, Khaloian-Sarnaghi A, van de Kuilen JW (2019) Numerical modelling of timber and timber joints: computational aspects. Wood Sci Technol 54(31):61. https://doi.org/10.1007/s00226-019-01142-8

Seeber F, Khaloian-Sarnaghi A, Rais A et al (2023) A numerical strength prediction approach for wood using elementwise local fiber directions from laser scanning. Mater Des 226:111578. https://doi.org/10.1016/j.matdes.2022.111578

Seeber F, Khaloian-Sarnaghi A, Yu T et al (2024) Development and validation of an orthotropic 3D elastoplastic damage model for wood, considering fiber deviations. Eng Struct 306:117928. https://doi.org/10.1016/j.engstruct.2024.117928

Seeber F, Khaloian-Sarnaghi A, Benvenuti E, van de Kuilen J-W (2025) Stress-gradient model for tensile damage in orthotropic materials. Compos Struct. https://doi.org/10.1016/j.compstruct.2025.119674

Shala S, Waisman H (2024) Localizing gradient damage model for anisotropic materials: focusing on timber. Int J Mech Sci 273:109207. https://doi.org/10.1016/j.ijmecsci.2024.109207

Simo JC, Ju JW (1989) Strain- and stress-based continuum damage models–i. Formulation. Math Comput Model 12(3):378. https://doi.org/10.1016/0895-7177(89)90117-9

Supriatna D, Yin B, Konopka D et al (2022) An anisotropic phase-field approach accounting for mixed fracture modes in wood structures within the representative crack element framework. Eng Fract Mech 269:108514. https://doi.org/10.1016/j.engfracmech.2022.108514

Tsai SW, Wu EM (1971) A general theory of strength for anisotropic materials. J Compos Mater. https://doi.org/10.21236/ADA306350

Voce E (1948) The relationship between stress and strain for homogeneous deformation. J Inst Met 74:537–562

Wang M, Song X, Gu X (2018) Three-dimensional combined elastic-plastic and damage model for nonlinear analysis of wood. J Struct Eng 144(8):04018103. https://doi.org/10.1061/(ASCE)ST.1943-541X.0002098

Zhang Y, Xu Y, Wang Y et al (2022) A simple implementation of localizing gradient damage model in Abaqus. Int J Damage Mech 31(10):1562–1591. https://doi.org/10.1177/10567895221109622

Authors and Affiliations

Franziska Seeber[1] · **Ani Khaloian-Sarnaghi**[1] · **Elena Benvenuti**[2] · **Jan-Willem van de Kuilen**[1,3]

✉ Franziska Seeber
seeber@hfm.tum.de

Ani Khaloian-Sarnaghi
khaloian@hfm.tum.de

Elena Benvenuti
elena.benvenuti@unife.it

Jan-Willem van de Kuilen
vandekuilen@hfm.tum.de

[1] School of Engineering and Design, Technical University of Munich (TUM), Arcisstr.21, Munich, Germany

[2] Engineering Department, University of Ferrara, via Saragat 1, Ferrara, Italy

[3] Faculty of Civil Engineering and Geosciences, Biobased Structures and Materials, Delft University of Technology, Stevinweg 1, Delft, The Netherlands